Hierarchical construction of higher-order exceptional points
Supplemental Material

Q. Zhong,[1,2] J. Kou,[3] Ş. K. Özdemir,[4] and R. El-Ganainy[1,2,*]

[1] *Department of Physics, Michigan Technological University, Houghton, Michigan 49931, USA*
[2] *Henes Center for Quantum Phenomena, Michigan Technological University, Houghton, Michigan 49931, USA*
[3] *Division of Engineering and Applied Science, California Institute of Technology, Pasadena, California 91125, USA*
[4] *Department of Engineering Science and Mechanics, and Materials Research Institute, The Pennsylvania State University, University Park, Pennsylvania 16802, USA*

A. Non-Hermitian J_x photonic array

As we mentioned in the main text, Hermitian J_x lattices have been studied previously in details [1–5]. Later on, non-Hermitian J_x arrays were introduced in [6]. Within the context of temporal coupled mode analysis, a PT symmetric J_x array made of N coupled optical resonators is described by the following system of equations:

$$i\frac{d\vec{c}}{dt} = H_N\vec{c}, H_N = \begin{bmatrix} ig_1 & \kappa_1 & \dots & 0 & 0 \\ & & \vdots & & \\ \dots & \kappa_{n-1} & ig_n & \kappa_n & \dots \\ & & \vdots & & \\ 0 & 0 & \dots & \kappa_{N-1} & ig_N \end{bmatrix}, \quad \text{(S1)}$$

where $\vec{c} = [c_1, c_2, ..., c_N]^T$ is the field amplitude vector, whereas $g_n = (2n - N - 1)\gamma$ and $\kappa_n = \sqrt{n(N-n)}\kappa$ are the gain/loss and coupling profiles. Here γ and κ are constant parameters, and $n = 1, 2, ..., N$. It is straightforward to show that the eigenvalues of the above system are given by [6]:

$$\lambda_n = (N - 2n + 1)\sqrt{\kappa^2 - \gamma^2}, \quad n = 1, 2, 3, ..., N. \quad \text{(S2)}$$

Moreover, by analyzing the structure of the associated eigenvectors [6], one can confirm that the point $\gamma = \kappa$ corresponds to an EP of order N.

B. Eigenvalues of Hamiltonian under perturbation

Here we sketch the derivation of the perturbative expression of Eq. (7) in the main text. The eigenvalues of $\mathcal{H}_4' = \mathcal{H}_4 + H_p - \omega_0 I$ are obtained by solving $|zI - \mathcal{H}_4'| = 0$, which gives the characteristic equation:

$$z^4 - 2\epsilon z^3 - 2i\gamma\epsilon z^2 - k\gamma^2\epsilon = 0. \quad \text{(S3)}$$

We are interested here in the small ϵ values. We thus employ a perturbation analysis based on Newton-Puiseux series, i.e. we expand $z = c_1\epsilon^{\frac{1}{4}} + c_2\epsilon^{\frac{2}{4}} + c_3\epsilon^{\frac{3}{4}} + ...$ By substituting back in Eq. (S3), and solving for the coefficients c's, we find $c_1 = i^{n-1}k^{\frac{1}{4}}\gamma^{\frac{1}{2}}$, $c_2 = 0$, and $c_3 = -\frac{1}{2}i^{-n}k^{-\frac{1}{4}}\gamma^{\frac{1}{2}}$.

* Corresponding author: ganainy@mtu.edu

C. Geometric and material parameters

For the full-wave simulations, we used the following parameters: each of the rings and the waveguides has a width $w = 0.25$ μm, and refractive indices of 3.47 in a background refractive index $n_0 = 1.44$ (relevant to SiN on silica platforms); the radii of the rings are identical and taken to be $R = 4.75$ μm each; the edge-to-edge separation between each ring and its neighbor waveguide is $h_1 = 0.25$ μm while that between the two rings is $h_2 = 0.4$ μm; the distance between the center of the nanoparticle and the edge of the ring resonator is 0.1 μm; and the distance between the ring-waveguide junction and the mirror is $L = 5.11$ μm. Moreover, the mirror is implemented by using a thin layer of silver with a thickness of 100 nm, and the loss and gain are modeled by including an imaginary part to the refractive index of the two microrings, i.e. $n_{1,2} = 3.47 \pm in_i$. Finally, the refractive index of the nanoparticle is $n_p = 3.47$. In order to minimize the effect of the surface roughness along the ring resonator due to numerical discretization, we set up the average mesh size equal to $\lambda/50$ (here $\lambda = \lambda_f/n$ where $\lambda_f = 1550$ nm is some free space reference wavelength and n is the refractive index of the materials) and use a finer mesh size of 1 nm around the nanoparticle region.

D. Optical parameters of the structure

In order to extract the numerical values of the various optical parameters, we first simulate a single microring resonator and compute its resonance frequency ω_0, or equivalently the corresponding free space wavelength of 1548 nm.

Next, we consider a coupled resonators configuration without any waveguides. In this case, the coupling coefficient between the resonators can be obtained by calculating the resonant frequencies of the even/odd supermodes in the absence of any gain or loss. By doing so using COMSOL software package, we find $\kappa = 98.8$ GHz. Next, we include the gain and loss in the two resonators by adding an imaginary part $\pm n_i$ to their refractive indices in order to create a PT symmetric arrangement and we plot the resonant frequency as a function of n_i as shown in Fig. S1. From these plots, we find that the EP occurs when $n_i = 2.9051 \times 10^{-4}$, which indicates that the

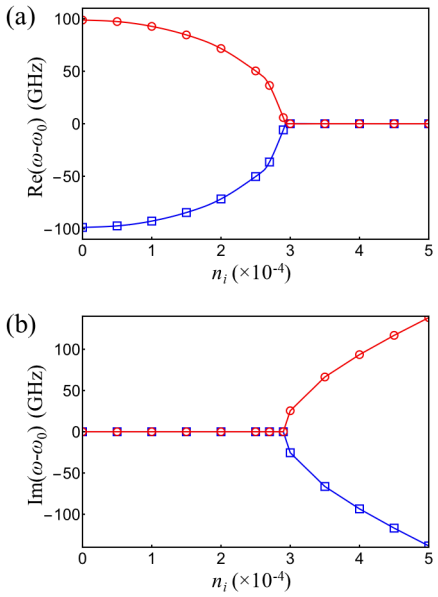

FIG. S1. Real (a) and imaginary (b) parts of the resonant frequencies ω of PT-symmetric resonators as a function of the imaginary part of the optical index n_i (see full description in the text) as obtained by full-wave simulations of the arrangement in Fig. 3 without the waveguide. The EP is located at $n_i = 2.9051 \times 10^{-4}$. The coupling coefficient between the two resonators can be obtained from the data at $n_i = 0$, which is found to be $\kappa = 98.8$ GHz.

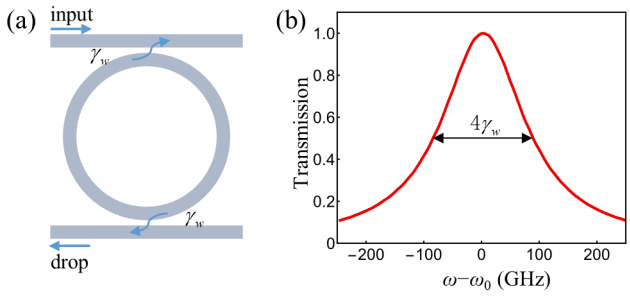

FIG. S2. (a) A microring resonator in add-drop configuration is used to evaluate the decay rate from the resonator. (b) Power transmission spectrum as obtained by using full-wave simulations gives a full-width at half-maximum bandwidth of $4\gamma_w = 173$ GHz.

field amplitude gain and loss at this point is equal to the coupling between the resonators.

Finally we evaluate the decay rate from the microring to the waveguide γ_w by constructing a symmetric add-drop ring resonator device and measuring the bandwidth of the transmission between the input and the output port as a function of frequency (Fig. S2(a)). In this case, for a negligible material absorption and radiation loss, the bandwidth is given by $BW = 4\gamma_w$. The FEM simulations gives the value $\gamma_w = 43.25$ GHz. Thus, for an all-pass ring-waveguide structure, the resonant frequency is complex and is given by $\omega_0 - i\gamma_w$.

E. Perturbation coefficient ϵ due to the nanoparticle

Here we characterize the perturbation ϵ introduced by the nanoparticle as a function of its radius R_p. To do so, we first note that a particle located in the near field of the microresonators will introduce a coupling between the CW and CCW modes, forming standing wave patterns. These new supermodes are distributed such that the particle is located at the node of the asymmetric mode, and at the maximum of the symmetric as shown in Fig. S3(a) for a 10 nm particle. Here symmetric and asymmetric refer to the field distribution with respect to a horizontal line that crosses the nanoparticle's center. Consequently, the asymmetric mode is not affected much by the particle while symmetric mode experiences a frequency shift of $2|\epsilon|$. The perturbation Hamiltonian H_p in the main text, which is written in the CW/CCW bases, capture this behavior. Finally, Fig. S3(b) plots the value of $|\epsilon|$

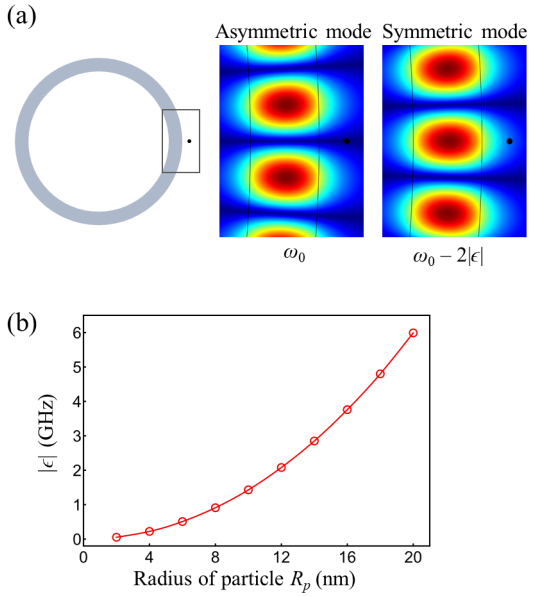

FIG. S3. A nanoparticle in the vicinity of a microring resonator (left panel of (a)) will introduce a coupling between the CW and CCW modes. The new supermodes of the ring will have symmetric/asymmetric field distribution with respect to the particle location. These modes are depicted in the right panel of (a) for a nanoparticle of radius 10-nm located at the node of the asymmetric mode and anti-node of the symmetric mode, respectively (the rest of the parameters as identical to those used in the text). (b) By using full-wave simulations to compute the frequency splitting due to nanoparticles and fitting these results to those obtained from the Hamiltonian H_{test}, we obtained the perturbation $|\epsilon|$ as a function of the particle's radii, R_p. (b) plots such a relation when R_p varies from 2 to 20 nm.

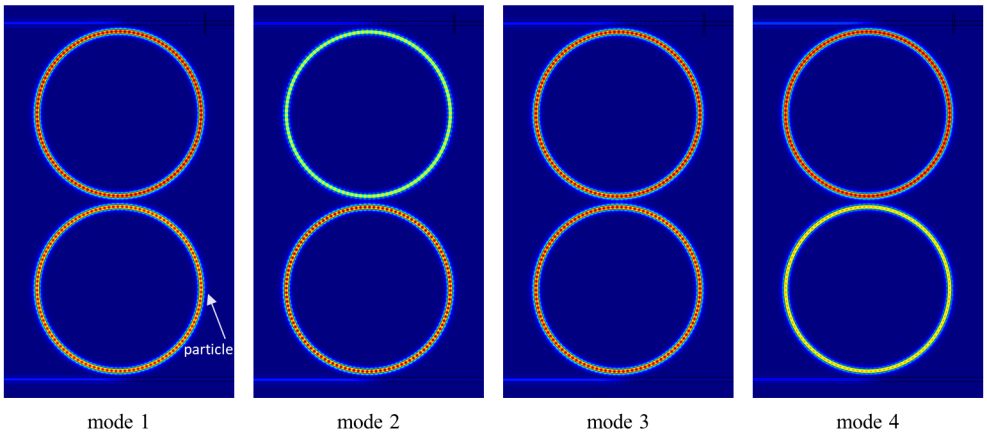

FIG. S4. Amplitude of the electric field distribution associated with the four eigenmodes of the structure for a nanoparticle with radius 10 nm. Note that mode 1 and 3 have nearly identical intensity in the two microring, consistent with their dominant real frequency shift. On the other hand, mode 2 has more intensity in the gain microring (bottom one), while mode 4 has more intensity in the lossy microring (top one), and as a result, they experience strong imaginary frequency shifts.

(the frequency is red-shifted because the particle's refractive index is larger than that of the surrounding [7]) as a function of R_p when the latter varies from 2 to 20 nm. In obtaining this plot, we fit the results obtained from full-wave simulations to those obtained using the Hamiltonian $H_{\text{test}} = \begin{pmatrix} \omega_0 + \epsilon & \epsilon \\ \epsilon & \omega_0 + \epsilon \end{pmatrix}$.

F. Modal profile

Figure S4 presents an example of the spatial field distribution (amplitude of the electric field) of the four eigenmodes of the structure for a particle of radius 10 nm. We observe that both eigenmodes 1 and 3 have equal power distribution in both rings, which explain their dominant real frequency splitting as demonstrated in Fig. 4(a). On the other hand, modes 2 and 4 have more intensity in the gain/loss microring, respectively which explain their dominant imaginary frequency shift as can be seen from Fig. 4(b). These numerical results thus confirm the analytical predictions and demonstrate the feasibility of our approach for practical implementations.

G. Further comments on the numerical results

By referring to Fig. 4(a) and (b) in the main text, we note that even in the absence of the particle, our simulations indicate a finite splitting between the eigenfrequencies. This is due to the fact that the waveguides themselves can introduce back-scattering between the modes. This means that our system operates in the vicinity, rather than exactly at, the EP. As indicated by Fig. 4(c), this does not have a significant impact on the ability of the structure to enhance light-matter interactions. Furthermore, a comparison between the numerical and analytical values for the splitting amplitudes (i.e. the value of the constant A in the formula $\text{Re}[\omega_1 - \omega_0] = A\epsilon^{0.24}$ and χ_1 in Eq. (7) in the main text confirms the excellent agreement with only 4% error.

[1] M. Christandl, N. Datta, A. Ekert, and A. J. Landahl, Phys. Rev. Lett. **92**, 187902 (2004).
[2] A. Perez-Leija, R. Keil, A. Kay, H. Moya-Cessa, S. Nolte, L.-C. Kwek, B. M. Rodríguez-Lara, A. Szameit, and D. N. Christodoulides, Phys. Rev. A **87**, 012309 (2013).
[3] A. Perez-Leija, R. Keil, H. Moya-Cessa, A. Szameit, and D. N. Christodoulides, Phys. Rev. A **87**, 022303 (2013).
[4] R. El-Ganainy, A. Eisfeld, M. Levy, and D. N. Christodoulides, Appl. Phys. Lett. **103**, 161105 (2013).
[5] R. J. Chapman, M. Santandrea, Z. Huang, G. Corrielli, A. Crespi, M.-H. Yung, R. Osellame, and A. Peruzzo, Nat. Commun. **7**, 11339 (2016).
[6] M. H. Teimourpour, R. El-Ganainy, A. Eisfeld, A. Szameit, and D. N. Christodoulides, Phys. Rev. A **90**, 053817 (2014).
[7] J. Zhu, Ş. K. Özdemir, Y.-F. Xiao, L. Li, L. He, D.-R. Chen, and L. Yang, Nat. Photon. **4**, 46 (2010).